# PCCP

## Accepted Manuscript

This is an *Accepted Manuscript*, which has been through the Royal Society of Chemistry peer review process and has been accepted for publication.

*Accepted Manuscripts* are published online shortly after acceptance, before technical editing, formatting and proof reading. Using this free service, authors can make their results available to the community, in citable form, before we publish the edited article. We will replace this *Accepted Manuscript* with the edited and formatted *Advance Article* as soon as it is available.

You can find more information about *Accepted Manuscripts* in the **Information for Authors**.

**ARTICLE TYPE**

# Dually Functional, N-doped Porous Graphene Foams as Counter Electrodes for Dye-sensitized Solar Cells

**Long Song,**[a] **Qiang Luo,**[b] **Fei Zhao,**[a] **Yang Li,**[a] **Hong Lin,**[b] **Liangti Qu**[a] **and Zhipan Zhang\***[a]

A series of nitrogen-doped porous graphene foams (NPGFs) have been prepared via hydrothermally treating the mixed solution of graphite oxide (GO) and ammonia. The NPGFs are employed as the counter electrode (CE) material for the dye-sensitized solar cells (DSCs) in conjunction with the conventional iodide-based electrolyte and the recently developed sulfide-based electrolyte. Tafel-
10 polarization tests and electrochemical impedance spectroscopic (EIS) measurements confirm the NPGFs work efficiently in both electrolyte systems and under AM 1.5G 100 mW cm$^{-2}$ light illumination, optimal efficiencies of 4.5% and 2.1% are obtained for the iodide-based electrolyte and sulfide-based electrolyte, respectively. To the best of our knowledge, this is the first study on N-doped graphene CEs in conjunction with the sulfide-based electrolytes and therefore, the current results are deemed to provide new insights
15 into developing novel low-cost and metal-free CEs for DSCs.

## Introduction

Since its first discovery in 2004,[1] graphene has attracted great theoretical and industrial interests. As a perfect flatland, graphene is a two-dimensional (2D) monoatomic-thick sheet of carbon
20 atoms arranged in the honeycomb pattern with large specific surface area, high intrinsic carrier mobility,[2–4] strong mechanical strength,[5] superior flexibility[6] and high chemical/thermal stability. While direct applications of 2D graphene sheets are unfortunately limited by their nature of easy aggregation and poor
25 dispersion in common solvents, building multidimensional functionalized graphene structures provides a practical avenue for mitigating these problems and demonstrating intriguing properties in imaging,[7] photonics[8] and various sensors.[9–11] In particular, the porous graphene framework renders an
30 interconnected network connecting all surface sites with fast electron transport and ample microporous/macroporous channels that facilitate the diffusion of guest molecules and electrolytes in the catalytic/electrochemical reactions,[12–14] making it an attractive platform to develop high-performance catalysts and
35 electrochemical devices.[15–17]

Owing to their low-cost production, simple fabrication, and high energy conversion efficiency, dye-sensitized solar cells (DSCs) are regarded as one of the most promising thin-film photovoltaic devices,[18] and today, champion cells of classical n-
40 type DSCs have reached a photo-to-electricity conversion efficiency of over 12%.[19] Under working conditions, the counter electrode (CE) plays a key role in regulating the DSCs device performance by constantly replenishing the reduced species of the redox couple, which is used as a mediator to regenerate the
45 sensitizer following the electron injection from the excited state of the sensitizer. As a result, the CE has to be highly catalytic to provide a cathodic current commensurate with the photocurrent generated by the working electrode. Platinum has long been selected as the catalyst on the CE owing to its high catalytic
50 activity and tolerance to the widely used triiodide/iodide-based electrolyte. However, Pt suffers from catalyst poisoning and is particularly less efficient when coupled with novel electrolytes involving sulfide redox couples.[20,21] In addition, as a noble metal, Pt is not attractive in industrial applications due to its limited
55 reserve and high price, leading to an extensive search for its abundant and low-cost alternatives.[22–28] Kay et al. first proposed a graphite powder/carbon black mixture as the CE[29] and stimulated vast research interests in carbon-based counter electrodes, such as activated carbon,[30] carbon black,[31] hard carbon spherule,[32]
60 fullerene,[33] carbon nanotubes,[34–40] and more recently graphene materials.[41–45] Particularly for graphene-based CEs, it is important to balance the electrical conductivity and the electrocatalytic activity of to improve the performance of the DSC. As the pristine graphene sheets are of low catalytic
65 activities due to the lack of active catalytic sites,[17] a range of heteroatoms such as oxygen, nitrogen, boron and sulfur have been introduced to dope the graphene material accordingly. Previous results have indicated that oxygen-doped graphene materials are usually of low electrical conductivity due to the
70 concomitant defects, while nitrogen-doped graphene can introduce electrocatalytic active sites with minimized damage to the conjugated structure of the graphitic basal plane and thus is potentially more catalytic and conductive.[46–50]

Aiming to profit from the desirable interfacial properties of
75 porous graphene network and the beneficial effects of nitrogen doping, we herein synthesize a series of N-doped porous graphene foams (NPGFs) with different nitrogen contents through a facile strategy by hydrothermally treating the mixture

of graphene oxide (GO) and ammonia. The obtained NPGFs are highly catalytic when used as the CEs for DSCs, rivalling the performance of the Pt CE in DSCs with the iodide-based electrolyte. More importantly, the CEs based on the NPGFs are

5 more compatible with sulfide-based electrolytes, superseding the Pt CE and leading to a 20% improvement in the light-to-electricity conversion efficiency under simulated AM 1.5G illumination at 100 mW cm$^{-2}$. The X-ray photoelectron spectroscopy (XPS) results show that the pyrrolic N and

10 quaternary N are mainly accounting for the catalytic activity, though the latter seems to play a more important role. The current work presents the first study on N-doped graphene CEs in conjunction with the sulfide-based electrolytes for DSCs and is thus expected to provide new insights in designing novel metal-

15 free, highly efficient CEs for DSC applications.

## Experimental

### Preparation of GO and NPGFs

GO was prepared by chemical oxidation and exfoliation of natural graphite under acidic conditions according to a modified

20 Hummer's method.[12] In order to dope the GO with nitrogen, 0.05 mL ammonia was added to 10 mL GO (2.8 mg mL$^{-1}$) and the mixture was hydrothermally treated to yield the sample of NPGF-1, where GO was believed to assemble into a porous graphene network and simultaneously become doped by the nitrogen

25 atom.[14,51] As the doping level may strongly influence the catalytic performance of the NPGF towards the redox reactions of the electrolyte, ammonia of different amounts of 0.5 mL and 2.5 mL were added to the same GO solution (10 mL, 2.8 mg mL$^{-1}$) and hydrothermally treated to give NPGF samples of NPGF-2 and

30 NPGF-3, respectively. In a typical experiment for preparing NPGF-2, 0.5 mL ammonia was added to 10.0 mL GO aqueous solution dropwise. The mixture was then stirred at 25 °C for 5 min and transferred into an autoclave under a hydrothermal treatment at 180 °C for 12 h. The solid product was finally

35 separated by centrifugation and washed with distilled water. The lyophilization was applied to prevent the aggregation of graphene sheets during drying process. For comparison, a control sample of reduced graphene oxide (rGO) was also prepared by treating the GO with the same hydrothermal procedure but in the absence of

40 any ammonia.

### Reagents and electrolytes

All chemicals and solvents used in the present work were of analytical grade. 1,3-dimethylimidazolium iodide (DMII), lithium iodide, lithium perchlorate, iodine, 4-*tert*-butylpyridine (*t*BP),

45 guanidinium thiocyanate (GuNCS) and acetonitrile were purchased from Sigma Aldrich (Shanghai, China). Fluorine-doped tin oxide (FTO) glass was purchased from Geao Education Equipment Co. Ltd. (Wuhan, China) and used as the conductive substrate. TiO$_2$ pastes of 20 nm and 200 nm particles were

50 purchased from HeptaChroma SolarTech (Dalian, China) and used as received. The iodide-based electrolyte (Electrolyte 1) contained 0.1 M 1,3-dimethylimidazolium iodide, 0.05 M LiI, 0.03 M I$_2$, 0.1 M guanidinium thiocyanate and 0.5 M 4-*tert*-butylpyridine in acetonitrile. For the sulfide-based electrolyte

55 (Electrolyte 2), a thiolate/disulfide (T$_2$/T$^-$) redox couple was selected and Electrolyte 2 was prepared by dissolving 0.4 M T$^-$,

0.4 M T$_2$, 0.5 M 4-*tert*-butylpyridine and 0.05 M LiClO$_4$ in the mixed solvent of acetonitrile/ethylene carbonate (volume ratio of 6:4), where T$^-$ and T$_2$ were synthesized according to a literature

60 method.[20] Additionally, a convenient aqueous sulfide/ polysulfide electrolyte composed of 1 M sulfur, 1 M Na$_2$S•9H$_2$O and 0.1 M NaOH in deionized water was used for the Tafel plot measurement.

### Spectroscopic measurements

65 The morphology of the samples was characterized by field-emission scanning electron microscopy (SEM, JSM-7001F) and transmission electron microscopy (TEM, JEM-2100). X-ray photoelectron spectroscopy (XPS) data were obtained with an ESCALab220i-XL electron spectrometer from VG Scientific

70 using 300W Al K$_\alpha$ radiation. Nitrogen adsorption–desorption isotherms were measured on a Quantachrome Autosorb-IQ gas adsorption analyzer at 77 K. Pore-size distribution and specific surface area were obtained through the non-local density functional theory (NLDFT) and the Brunauer–Emmett–Teller

75 (BET) methods from the adsorption branch of the isotherm at a relative pressure range of p/p$_0$ = 0.05–0.25.

For photoelectrochemical measurements, a 450 W xenon light source solar simulator (Oriel, model 9119) with AM 1.5G filter (Oriel, model 91192) was used to give an irradiance of 100 mW

80 cm$^{-2}$ at the surface of the solar cell. The current-voltage (*I-V*) characteristics of the cell under these conditions were obtained by applying external potential bias to the cell and measuring the generated photocurrent with a Keithley model 2400 digital sourcemeter (Keithley, USA).

85 Electrochemical measurements were performed on a computer-controlled potentiostat equipped with a frequency response analyzer (Autolab, Model 204). Tafel plots were obtained by cycling symmetrical dummy cells assembled with two identical CEs within the potential range of -0.8 to 0.8 V at a scan rate of 10

90 mV s$^{-1}$. For the impedance measurement, the frequency range is 0.01-100 KHz and the magnitude of the modulation signal is 10 mV. The obtained spectra were fitted with Z-View software (v2.8b, Scribner Associates Inc.) in terms of appropriate equivalent circuits.

95 ### Device Fabrication

A typical double-layer TiO$_2$ mesoscopic film was used as the photoanode. A 7 μm-thick transparent layer of 20 nm-sized TiO$_2$ particles was first screen-printed on the FTO conducting glass electrode and further coated with a 5 μm-thick second layer of

100 200 nm-sized light scattering anatase particles. The double-layer structured TiO$_2$ electrode was then sintered at 500 °C for 30 minutes and cooled to about 100 °C in air before it was then immersed in the 0.3 mM N719 dye (HeptaChroma SolarTech) solution at room temperature for 16 h. The Pt CE was prepared

105 by homogeneously dispensing 5 mM H$_2$PtCl$_6$ isopropanol solution on the FTO glass and annealing the FTO glass in air at 450 °C for 15 min by a heat gun (Liester, Switzerland). To prepare the NPGF CEs, the NPGF was first dispersed in DMF solution to give a 5 mg mL$^{-1}$ paste with 10% Nafion (volume

110 ratio) added. The mixed solution was then applied on the FTO glass, followed by annealing in air at 450 °C for 30 min.

To assemble the DSC, the sensitized TiO$_2$ film electrode and the CE were separated by a 52 μm-thick Surlyn hot-melt ring

(DuPont, USA) and sealed by press-heating. The internal space was evacuated by vacuum and then filled with the electrolyte through a filling hole made by a sandblasting drill in the back of the CE glass substrate, before the hole was finally sealed with a
5 Surlyn sheet under a thin glass cover by heating.

## Results and discussion

The morphology of the NPGF samples is first characterized with the scanning electron microscopy (SEM) and transmission electron microscopy (TEM). Fig. 1a and 1b are the representative
10 SEM images of the NPGF-2 and rGO, respectively. Compared to the porous three-dimensional architecture of the rGO, the NPGF-2 more features a film-like structure with micro-sized channels. Enlarged views of NPGF-2 (Fig. 1c) and rGO (Fig. 1d) both show a rough surface where mesopores appear to be visible. The
15 TEM image (Fig. 1e) suggests the NPGF-2 has a more wrinkled surface in comparison to the rGO (Fig. 1f), probably arising from the defective nature caused by the ammonia treatment. The specific surface area and pore size distributions are measured by the isotherms of $N_2$ adsorption-desorption. As shown in Fig. 1g,
20 both rGO and NPGFs show Type IV isotherm characteristics with a wide hysteresis loop, indicating the existence of abundant mesopores. The Brunauer-Emmett-Teller (BET) surface area of rGO, NPGF-1, NPGF-2 and NPGF-3 is 439, 502, 479 and 516 $m^2$ $g^{-1}$, respectively, and the pore size distribution curves in Fig. 1h
25 reveal a narrow distribution of pores with diameters ranging from 1 to 4 nm for rGO and different NPGFs, where the nitrogen doping seems to enhance the presence of small pores. Overall, with a barely changed pore size distribution, the NPGFs are of around 10 to 15% higher specific surface area than that of the
30 rGO, therefore rendering a large electrode/electrolyte interface that could contribute to an efficient catalysis on the redox reaction of the electrolyte.
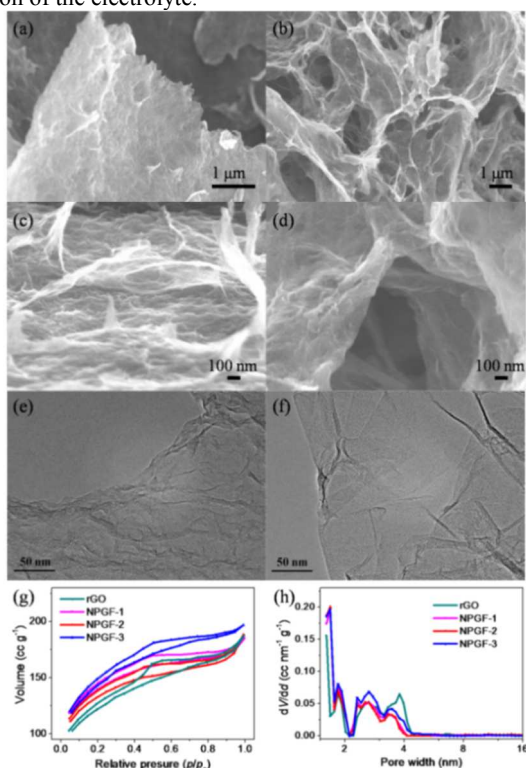


**Fig. 1.** The SEM images of the NPGF-2 (a, c) and (b, d) rGO, where the scale
35 bars are 1 μm, 1 μm, 100 nm and 100 nm, respectively. (e) The TEM images of the NPGF-2 and (f) rGO, with the scales bars of 50 nm. (g) The $N_2$ adsorption-desorption isotherms and (h) pore size distributions of the rGO, NPGF-1, NPGF-2 and NPGF-3, respectively.

The X-ray photoelectron spectroscopy (XPS) was selected to
40 probe the doping level of the NPGF samples. As demonstrated in Fig. 2a, the XPS survey spectrum of NPGF-1 confirms the presence of C1s, O1s, and N1s without any impurities. The inset of Fig. 2a specifies the atomic percentage of the elements and the calculated nitrogen to carbon (N/C) atomic ratio is about 8.85%.
45 The high-solution of C1s spectrum of NPGF-1 (Fig. 2b) shows characteristic features from the $sp^2$-hybridized graphitic carbon (284.8 eV), C-N-C (285.2 eV), C=O (288.3 eV) and O-C=O (290.3 eV), respectively, indicating the heteroatom nitrogen has successfully been incorporated into the graphene basal plane
50 without resorting to the energy-consuming high-temperature doping process.[48-50] Meanwhile, the high-resolution of N1s spectrum of NPGF-1, NPGF-2 and NPGF-3 (Fig. 2c to 2f) can be separated into contributions from four kinds of nitrogen atoms, namely pyridinic N (398.1 eV), pyrrolic N (399.3 eV), quaternary
55 N (400.8 eV) and pyridinic N-oxide (403.7 eV), respectively. The exact atomic ratios of the four N species to the carbon atoms are summarized in Fig. 2f. In general, the total N/C ratio in the graphite network rises with the increasing amount of ammonia in the precursor solution, and the N/C ratio can reach as high as
60 11.65%. However, the relative ratio of individual N species apparently differs from NPGF-1 to NPGF-3, implying the catalytic activity of different NPGF samples would be considerably different when used as CEs to catalyze the redox reaction of the electrolyte in the DSCs (*vide infra*).
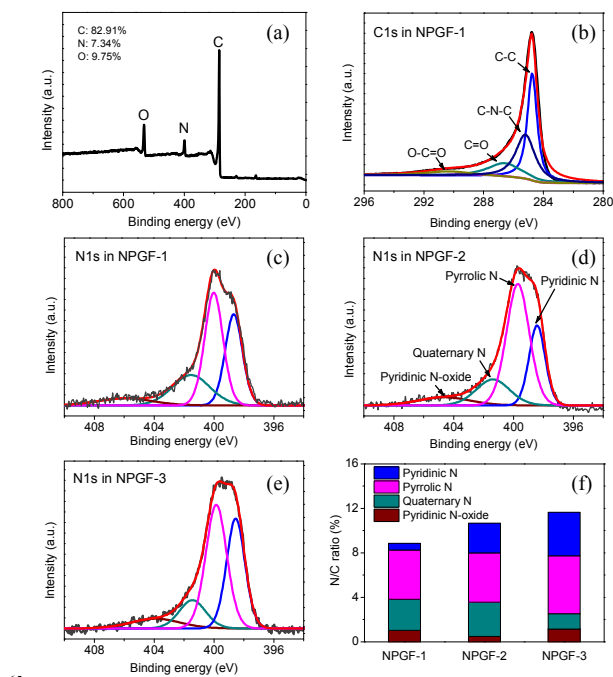


65
**Fig. 2.** XPS spectra of the NPGF-1, NPGF-2 and NPGF-3. (a) Survey, (b) high-resolution C1s and (c) N1s spectra of the NPGF-1. High-resolution N1s spectra of (d) NPGF-2 and (e) NPGF-3. (f) The relative N/C ratio distributions of individual nitrogen species.

The efficacy of the NPGF as the CE is first evaluated with Tafel-polarization and electrochemical impedance spectroscopic (EIS) measurements on symmetrical dummy cells fabricated with two identical CEs in conjunction with Electrolyte 1 that is based on the widely used $I^-/I_3^-$ redox couple. Fig. 3a plots the Tafel curves of the dummy cells fabricated of Pt, rGO and different NPGF CEs, with the logarithmic current density (Log $J$) presented as a function of the applied bias. The rGO is apparently of a poor catalytic performance to the redox reaction of $I^-/I_3^-$, where a bias of at least 140 mV is needed to drive a mere current density of 1 mA cm$^{-2}$. In comparison, the N-doping considerably improves the catalytic current density and the bias for attaining 1 mA cm$^{-2}$ is 54 mV and 40 mV for the NPGF-1 and NPGF-3 electrodes, respectively. Impressively, this bias is further reduced to 33 mV for the NPGF-2 electrode, very close to that of the Pt CE (28 mV), suggesting that the NPGF-2 can effective catalyze the redox reaction of $I^-/I_3^-$ as effectively as the Pt electrode. This is further demonstrated in the EIS spectra of these dummy cells measured at open circuit with a modulating amplitude of 10 mV (Fig. 3b). The obtained Nyquist plots typically comprise two characteristic semicircles corresponding to the charge-transfer resistance ($R_{ct}$) of the redox reaction at the CE/electrolyte interface at high frequency regions and the Warburg impedance associated with the Nerstian diffusion of the redox couple in the electrolyte solution at low frequency regions, respectively. The charge-transfer resistance $R_{ct}$ related to the heterogeneous electron exchange involving the $I_3^-\leftrightarrow I^-$ redox couple at the electrolyte/CE interface is normally given for the equilibrium potential. From the Bulter-Volmer equation with no mass-transfer effects, one obtains

$$R_{ct} = \frac{RT}{nF} \cdot \frac{1}{J_0 A} \qquad (1)$$

where $R$ is the molar gas constant, $T$ is the temperature, $F$ is the Faraday constant, $A$ the electrode area, $n$ is the mole number of electrons involved in the reaction and $J_0$ is the exchange current density of the reaction, respectively. Table 1 compares the values of $R_{ct}$ and the calculated $J_0$ for dummy cells fabricated of Pt, rGO and different NPGF CEs. The rGO CE shows the largest $R_{ct}$ of 128.8 ohm cm$^2$, suggesting it is least active in catalyzing the $I^-/I_3^-$ redox reaction. In consistence with the results from the Tafel polarization, the N-doping significantly increases the catalytic activity of the graphene CEs and $R_{ct}$ for the NPGF-1 and NPGF-3 decreases to 40.5 and 15.9 ohm cm$^2$, respectively. Again, the NPGF-2 has an even smaller $R_{ct}$ of 15.2 ohm cm$^2$, approaching that of the Pt CE (9.8 ohm cm$^2$) and manifesting its good catalytic activity towards the $I^-/I_3^-$ redox couple. The calculated exchange current density ($J_{0,calc}$) is 0.10 mA cm$^{-2}$ for the rGO CE, increasing to close to 1 mA cm$^{-2}$ with the nitrogen doping. As Equation 1 considers no mass-transfer effects and the difference between diffusion coefficients of $I_3^-$ and $I^-$, the expected $J_{0,calc}$ values in Table 1 are slightly larger than those found in the Tafel polarization curves shown in Fig. 3a. Nevertheless, it is more important that the sequence of the catalytic activity remains $J_0$(rGO) << $J_0$(NPGF-1) < $J_0$(NPGF-3) < $J_0$(NPGF-2), in a good agreement with the results from the Tafel polarization curves in Fig. 3a.
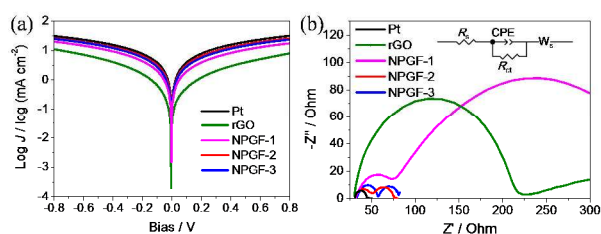


**Fig. 3.** (a) Tafel polarization plots and (b) open-circuit EIS spectra of symmetrical dummy cells fabricated from Pt, rGO and NPGF CEs. The inset of (b) shows the equivalent circuit of the dummy cell, where the $R_s$, $R_{ct}$, CPE and $W_s$ are the serial resistance of the cell, the charge-transfer resistance at the CE/electrolyte interface and the constant phase element modeling the behavior of the double layer and the Warburg impedance component associated with the diffusion of the electrolyte, respectively.

**Table 1.** The charge-transfer resistance and calculated exchange current densities ($J_{0,calc}$) of the symmetrical dummy cells fabricated by Pt, rGO and NPGF CEs with electrolytes containing $I^-/I_3^-$ and $S^{2-}/S_n^{2-}$ redox couples. $J_{0,calc}$ is calculated by Equation 1 and for simplicity, the mole number of electrons involved in the $S^{2-}/S_n^{2-}$ couple is selected to be 2. The EIS spectra are measured at open circuit and the electrode area is 0.72 cm$^2$

| CE materials | $I^-/I_3^-$ couple | | $S^{2-}/S_n^{2-}$ couple | |
|---|---|---|---|---|
| | $R_{ct}$ (Ohm cm$^2$) | $J_{0,calc}$ (mA cm$^{-2}$) | $R_{ct}$ (Ohm cm$^2$) | $J_{0,calc}$ (mA cm$^{-2}$) |
| Pt | 9.8 | 1.31 | 3615.9 | 0.004 |
| rGO | 128.8 | 0.10 | 553.1 | 0.02 |
| NPGF-1 | 40.5 | 0.32 | 23.4 | 0.55 |
| NPGF-2 | 15.2 | 0.85 | 12.1 | 1.06 |
| NPGF-3 | 15.9 | 0.81 | 28.5 | 0.45 |

Iodine-free redox couples have been widely investigated as alternatives for the conventional $I^-/I_3^-$ redox shuttle in DSCs, mainly motivated by desires to overcome its disadvantages such as large thermodynamic energy loss in the dye regeneration process, excessive visible light absorption and corrosiveness towards current-collecting metal grids.[23] Therefore, it would be natural to study if the NPGFs would be compatible with other redox couples such as the recently discovered sulfide-based electrolyte.[20,27] A convenient aqueous electrolyte that is based on sulfide/polysulfide ($S^{2-}/S_n^{2-}$) redox couple and commonly used in the quantum-dot sensitized solar cells was selected to use in the symmetrical dummy cells made from Pt, rGO and different NPGF CEs for conducting the Tafel polarization and EIS measurements (Fig. 4). Pt has long been identified as a poor catalyst for sulfide-based electrolyte probably due to the poisoning effect and thus associated with substantial overpotentials for the sulfide regeneration, as is also reflected in Fig. 4a where a bias of at least 190 mV is needed to drive a current density of 1 mA cm$^{-2}$. In comparison, all graphene CEs apparently exhibit higher catalytic activities and the overpotential for attaining 1 mA cm$^{-2}$ reduces to 106, 74, 50 and 62 mV for rGO, NPGF-1, NPGF-2 and NPGF-3 CEs, respectively. Interestingly, even the undoped rGO is more catalytic towards the redox reaction of $S^{2-}/S_n^{2-}$, validating that the graphene CEs are better catalysts in conjunction with the sulfide-based electrolyte. This is further confirmed by the corresponding EIS spectra plotted in Fig. 4b, where the Pt CE shows a huge $R_{ct}$ of 3615.9

ohm cm$^2$ due to the poor activity. In sharp contrast, the $R_{ct}$ of the rGO, NPGF-1 and NPGF-3 CEs is 553.1, 23.4 and 28.5 ohm cm$^2$, respectively. The NPGF-2 CE has a $R_{ct}$ as low as 12.1 ohm cm$^2$, highlighting its excellent catalytic performance towards the S$^{2-}$ /S$_n^{2-}$ redox couple.
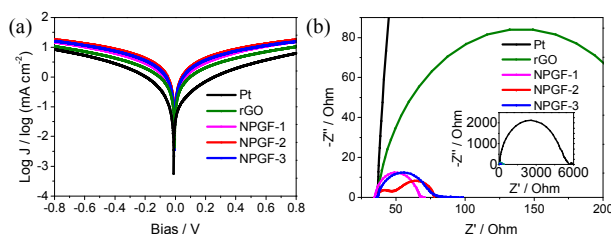


**Fig. 4**. (a) Tafel polarization curves and (b) EIS spectra of the symmetrical dummy cells fabricated with Pt, rGO and different NPGF CEs in conjunction with the aqueous sulfide/polysulfide electrolyte. The inset of (b) shows the full-scale Nyquist plot of the Pt CE.

The observed superior catalytic activity of NPGF-2 over those of NPGF-1 and NPGF-3 has motivated us to study the origin of its excellent performance towards both iodide-based and sulfide-based electrolytes. Compared to NPGF-1 and NPGF-3, NPGF-2 has a slightly lower specific surface area (479 *versus* 502 and 516 m$^2$ g$^{-1}$, Fig. 1g) and a similar pore size distribution (Fig. 1h), suggesting that the improvement in the catalytic performance observed in NPGF-2 should originate from its N-doping nature rather than the specific surface area and pore morphology. It has been proposed that the catalytic activity of N-doped graphene is induced by the increased electron/spin density and thus directly associated with the relative content of pyridinic N, pyrrolic N, quaternary N and pyridinic N-oxide. Hou et al. suggested that the pyridinic N and quaternary N can serve as active sites for iodine reduction with the catalytic activity following the tendency of the total content of the pyridinic N and quaternary N, while the pyrrolic N is far inferior and the N-oxide of pyridinic N-oxide is even not responsible for the catalytic activity.[50] The detailed atomic ratios of individual N species in the NPGF-1, NPGF-2 and NPGF-3 samples determined from the XPS results (Fig. 2f) are listed in Table 2. The content of the pyridinic N follows a monotonic increase from the NPGF-1 to NPGF-3 with the increasing ammonia amount used in the precursor solution, while the content of the quaternary N rises first and then declines. Additionally, though the NPGF-3 features the highest overall N/C ratio, the N atoms mostly exist in the form of inactive pyrrolic N. Consequently, the NPGF-2 clearly has a higher total content of the pyridinic N and quaternary N, negating the adverse effect of its slightly lower specific surface area than those of the NPGF-1 and NPGF-3 and eventually leading to the observed better catalytic activity. Meanwhile, the inferior electrocatalytic activity of the NPGF-3 to that of the NPGF-1 towards the sulfide-based electrolyte seems to imply the quaternary N is the main catalytic site for the redox reaction between S$^{2-}$ and S$_n^{2-}$. As the content of the individual N content could be preferentially altered by judicious selection of the synthetic route such as space-confinement-induced preparation,[52] the current result is important for developing the next generation of highly active metal-free DSC CEs towards sulfide electrolytes.

**Table 2.** The relative atomic ratios of individual nitrogen species in different NPGFs.

| CE materials | N/C ratio (%) | | | |
|---|---|---|---|---|
| | Pyridinic N | Quaternary N | Pyrrolic N | Pyridinic N-oxide |
| NPGF-1 | 0.60 | 2.78 | 4.43 | 1.04 |
| NPGF-2 | 2.67 | 3.08 | 4.42 | 0.50 |
| NPGF-3 | 3.91 | 1.36 | 5.22 | 1.16 |

We finally access the performance of the NPGF CEs in the full DSC devices. Figure 5a compares the *I-V* characteristics of N-719 sensitized DSCs made with the NPGF-2 CE and Pt CE in conjunction with the iodide-based Electrolyte 1 under the simulated AM 1.5G illumination at 100 mW cm$^{-2}$ (1 sun) and the photovoltaic parameters are listed in Table 3. The DSC with the NPGF-2 CE shows a short-circuit current density ($J_{sc}$) of 13.1 mA cm$^{-2}$, an open-circuit voltage ($V_{oc}$) of 710 mV and a fill factor (*FF*) of 0.48, reaching a photo-to-electric conversion efficiency ($\eta$) of 4.5%. In comparison, the $\eta$ of the DSC with the Pt CE is 4.9%, mainly due to the improvement in the $J_{sc}$ from 13.1 mA cm$^{-2}$ to 14.6 mA cm$^{-2}$ and $V_{oc}$ from 710 mV to 750 mV. The case is a bit different when the Electrolyte 2 based on the thiolate/disulfide (T$^-$/T$_2$) couple is used. As plotted in Figure 5b, the $J_{sc}$, $V_{oc}$, *FF* and $\eta$ of the DSC with the Pt CE is 8.40 mA cm$^{-2}$, 602 mV, 0.35 and 1.75%, respectively. When the NPGF-2 CE is used, the *FF* of the DSC considerably improves to 0.50, offsetting the slight decrease in the $J_{sc}$ and leading to a higher conversion efficiency of 2.1% at 1 sun. Therefore, the NPGF-2 CE could approach Pt with the triiodide/iodide redox couple used and even supersede Pt when the T$^-$/T$_2$ electrolyte is employed, proving its great potential as the alternative metal-free CE for DSCs instead of the conventional noble metal catalyst.
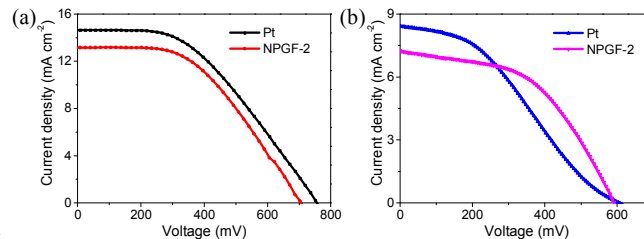


**Figure 5.** *I-V* curves for DSCs fabricated with the NPGF-2 and Pt CEs using (a) the triiodide/iodide electrolyte and (b) T$^-$/T$_2$ electrolyte, respectively.

**Table 3.** Photovoltaic parameters of the DSCs fabricated with the NPGF-2 and Pt CEs using the triiodide/iodide electrolyte and T$^-$/T$_2$ electrolyte.

| Device ID | $J_{sc}$ (mA cm$^{-2}$) | $V_{oc}$ (mV) | FF | $\eta$ (%) |
|---|---|---|---|---|
| Pt (I$^-$/I$_3^-$) | 14.64 | 756 | 0.45 | 4.9 |
| NPGF-2 (I$^-$/I$_3^-$) | 13.14 | 708 | 0.48 | 4.5 |
| Pt (T$^-$/T$_2$) | 8.40 | 602 | 0.35 | 1.7 |
| NPGF-2 (T$^-$/T$_2$) | 7.22 | 591 | 0.50 | 2.1 |

## Conclusions

In summary, we have developed a low-cost and convenient solution process to prepare the nitrogen-doped porous graphene foams as efficient counter electrode materials for the DSCs. Tafel polarization and EIS experiments confirm the N-doped porous graphene foams are highly catalytic towards both the conventional triiodide/iodide electrolyte and the sulfide-based electrolyte, and a medium ammonia content in the precursor

solution is found to yield the best CE of NPGF-2 due to the maximized total content of the pyridinic N and quaternary N. The conversion efficiency of the DSC with the NPGF-2 CE is slightly inferior to that of the DSC with the Pt CE in the case of triiodide/iodide electrolyte, but it supersedes that of the DSC with the Pt CE when the sulfide-based $T^-/T_2$ electrolyte is employed. The current results unambiguously demonstrate that the NPGF-2 is an excellent metal-free CE particularly for the sulfide electrolyte, rendering new insights into designing next-generation and highly-efficient CEs for DSCs with even a lower cost.

## Acknowledgements

## Notes and references

*[a] Key Laboratory of Cluster Science, Ministry of Education of China Beijing Key Laboratory of Photoelectric/Electrophotonic Conversion Materials, School of Chemistry, Beijing Institute of Technology, Beijing 100081, P. R. China. Tel: +86-10-68918608; E-mail: Zhipan@bit.edu.cn*
*[b] Department of Material Science and Engineering, Tsinghua University, Beijing 100084, P. R. China*

1   K.S. Novoselov, A.K. Geim, S.V. Morozov, D. Jiang, Y. Zhang, S.V. Dubonos, I.V. Grigorieva and A.A. Firsov, *Science*, 2004, **306**, 666.
2   K.I. Bolotin, K.J. Sikes, Z. Jiang, M. Klima, G. Fudenberg, J. Hone, P. Kim and H.L. Stormer, *Solid State Commun.*, 2008, **146**, 351.
3   S.V. Morozov, K.S. Novoselov, M.I. Katsnelson, F. Schedin, D.C. Elias, J.A. Jaszczak and A.K. Geim, *Phys. Rev. Lett.*, 2008, **100**, 016602.
4   X. Du, I. Skachko, A. Barker and E.Y. Andrei, *Nat. Nanotechnol.*, 2008, **3**, 491.
5   T.J Booth, P. Blake, R.R Nair, D. Jiang, E.W. Hill, U. Bangert, A. Bleloch, M. Gass, K.S. Novoselov, M.I. Katsnelson and A.K. Geim, *Nano Lett.*, 2008, **8**, 2442.
6   Z.L. Dong, C.C. Jiang, H.H. Cheng, Y. Zhao, G.Q. Shi, L. Jiang and L.T. Qu, *Adv. Mater.*, 2012, **24**, 1856.
7   J. Shen, Y. Zhu, X. Yang and C. Li, *Chem. Commun.*, 2012, **48**, 3686.
8   Q.L. Bao and K.P. Loh, *ACS Nano*, 2012, **6**, 3677.
9   T. Kuila, S. Bose, P. Khanra, A.K. Mishra, N.H. Kim and J.H. Lee, *Biosens. Bioelectron.*, 2011, **26**, 4637.
10  Y.X. Liu, X.C. Dong and P. Chen, *Chem. Soc. Rev.*, 2012, **41**, 2283.
11  Q.Y. He, S.X. Wu, Z.Y. Yin and H. Zhang, *Chem. Sci.*, 2012, **3**, 1764.
12  C.G. Hu, H.H. Cheng, Y. Zhao, Y. Hu, Y. Liu, L.M. Dai and L.T. Qu, *Adv. Mater.*, 2012, **24**, 5493.
13  Y. Zhao, J. Liu, Y. Hu, H.H. Cheng, C.G. Hu, C.C. Jiang, L. Jiang, A.Y. Cao and L.T. Qu, *Adv. Mater.*, 2013, **25**, 591.
14  Y. Zhao, C.G. Hu, Y. Hu, H.H. Cheng, G.Q. Shi and L.T. Qu, *Angew. Chem. Int. Ed.*, 2012, **51**, 11533.
15  C. Li and G.Q. Shi, *Nanoscale*, 2012, **4**, 5549.
16  S.J. Guo and S.J. Dong, *Chem. Soc. Rev.*, 2011, **40**, 2644.
17  C.C. Huang, C. Li and G.Q. Shi, *Energy Environ. Sci.*, 2012, **5**, 8848.
18  B. O'Regan and M. Grätzel, *Nature*, 1991, **353**, 737.
19  A. Yella, H.W. Lee, H.N. Tsao, C.Y. Yi, A.K. Chandiran, M.K. Nazeeruddin, E.W. Diau, C.Y. Yeh, S.M. Zakeeruddin and M. Grätzel, *Science*, 2011, **334**, 629.
20  M.K. Wang, N. Chamberland, L. Breau, J.E. Moser, R. Humphry-Baker, B. Marsan, S.M. Zakeeruddin and M. Grätzel, *Nat. Chem.*, 2010, **2**, 385.
21  Y.R. Liu, J.R. Jennings, M. Parameswaran and Q. Wang, *Energy Environ. Sci.*, 2011, **4**, 564.
22  T.N. Murakami and M. Grätzel, *Inorg. Chim. Acta*, 2008, **361**, 572.
23  G. Boschloo and A. Hagfeldt, *Acc. Chem. Res.*, 2009, **42**, 1819.
24  S. Yanagida, Y.H. Yu and K. Manseki, *Acc. Chem. Res.*, 2009, **42**, 1827.
25  L.J. Brennan, M.T. Byrne, M. Bari and Y.K. Gun'ko, *Adv. Energy. Mater.*, 2011, **1**, 472.
26  M.X. Wu and T.L. Ma, *Chemsuschem*, 2012, **8**, 1343.
27  F. Hao, P. Dong, Q. Luo, J.B. Li, J. Lou and H. Lin, *Energy Environ. Sci.*, 2013, **6**, 2003.
28  S. Ahmad, E. Guillen, L. Kavan, M. Grätzel and M.K. Nazeeruddin, *Energy Environ. Sci.*, 2013, **6**, 3439.
29  A. Kay and M. Grätzel, *Sol. Energy Mater. Sol. Cells*, 1996, **44**, 99.
30  K. Imoto, K. Takahashi, T. Yamaguchi, T. Komura, J. Nakamura and K. Murata, *Sol. Energy Mater. Sol. Cells*, 2003, **79**, 459.
31  T.N. Murakami, S. Ito, Q. Wang, M.K. Nazeeruddin, T. Bessho, I. Cesar, P. Liska, R. Humphry-Baker, P. Comte, P. Péchy and M. Grätzel, *J. Electrochem. Soc.*, 2006, **153**, A2255.
32  Z. Huang, X.Z. Liu, K.X. Li, D.M. Li, Y.H Luo, H. Li, W.B. Song, L.Q. Chen and Q.B. Meng, *Electrochem. Commun.*, 2007, **9**, 596.
33  T. Hino, Y. Ogawa and N. Kuramoto, *Carbon*, 2006, **44**, 880.
34  Q.W. Jiang, G.R. Li, F. Wang and X.P. Gao, *Electrochem. Commun.*, 2010, **12**, 924.
35  K. Suzuki, M. Yamaguchi, M. Kumagai and S. Yanagida, *Chem. Lett.*, 2003, **32**, 28.
36  E. Ramasamy, W.J. Lee, D.Y. Lee and J.S. Song, *Electrochem. Commun.*, 2008, **10**, 1087.
37  W.J. Lee, E. Ramasamy, D.Y. Lee and J.S. Song, *ACS Appl. Mater. Interfaces*, 2009, **1**, 1145.
38  J. Han, H. Kim, D.Y. Kim, S.M. Jo and S.Y. Jang, *ACS Nano*, 2010, **4**, 3503.
39  X. Mei, S.J. Cho, B. Fan and J. Ouyang, *Nanotechnology*, 2010, **21**, 395202.
40  F. Hao, P. Dong, J. Zhang, Y.C. Zhang, P.E. Loya, R.H. Hauge, J.B. Li, J. Lou and  H. Lin, *Sci. Rep.*, 2012, **2**, 368.
41  Y.X. Xu, H. Bai, G.W. Lu, C. Li and G.Q. Shi, *J. Am. Chem. Soc.*, 2008, **130**, 5856.
42  L. Kavan, J.H. Yum and M. Grätzel, *Nano Lett.*, 2011, **11**, 5501.
43  R. Cruz, D. Alfredo, P. Tanaka and A. Mendes, *Sol. Energy*, 2012, **86**, 716.
44  D.W. Zhang, X.D. Li, H.B. Li, S. Chen, Z. Sun, X.J. Yin and S.M. Huang, *Carbon*, 2011, **49**, 5382.
45  H. Wang and Y.H. Hu, *Energy Environ. Sci.*, 2012, **5**, 8182.
46  L.T. Qu, Y. Liu, J.B. Baek and L.M. Dai, *ACS Nano*, 2010, **4**, 1321.
47  H.B. Wang, T. Maiyalagan and X. Wang, *ACS Catal.*, 2012, **2**, 781.
48  M.J. Ju, J.C. Kim, H.J. Choi, I.T. Choi, S.G. Kim, K. Lim, J.J. Ko, J.J. Lee, I.Y. Jeon, J.B. Baek and H.K. Kim,, *ACS Nano*, 2013, **7**, 5243.
49  Y.H. Xue, J. Liu, H. Chen, R.G. Wang, D.Q. Li and J. Qu, *Angew. Chem. Int. Ed.*, 2012, **51**, 12124.
50  S.C. Hou, X. Cai, H.W. Wu, X. Yu, M. Peng, K. Yan and D.C. Zou, *Energy Environ. Sci.*, 2013, **6**, 3356.
51  P. Chen, T.Y. Xiao, Y.H. Qian, S.S. Li and S.H. Yu, *Adv. Mater.*, 2013, **25**, 3192.
52  W. Ding, Z.D. Wei, S.G. Chen, X.Q. Qi, T. Yang, J.S. Hu, D. Wang, L.J. Wan, S.F. Alvi and L. Li, *Angew. Chem. Int. Ed.*, 2013, **52**, 11755.